Impact of coherent coupling of plasmonic dipole modes in far-field scattering of templated metallic nanoislands

Seyed M. Sadeghi * and Dustin T. Roberts
Department of Physics and Astronomy, University of Alabama in Huntsville, Huntsville, Alabama 35899, USA

(Received 6 April 2023; accepted 27 July 2023; published 16 August 2023)

Two-dimensional periodic arrays of regions containing metallic nanoislands with random sizes and shapes, known as templated nanoisland arrays, can exhibit plasmonic phase-correlated dipole domains. These domains emerge at specific wavelengths where the lattice-induced plasmon dipoles of the nanoislands are coherently coupled together, forming collective plasmonic states that extend spatially over each region with scales of up to one micron S. M. Sadeghi and R. R. Gutha, Phys. Rev. Appl. **15**, 034018 (2021). In this paper, we demonstrate that the far-field in-plane scattering of these arrays can be utilized to access the coherent signatures of the plasmonic phase-correlated dipole domains. Our results reveal that this process is particularly pronounced when the coherent coupling of these domains, facilitated by their hybridization with the Rayleigh Anomaly, gives rise to surface lattice resonances. These resonances effectively enhance the far-field in-plane scattering of templated nanoisland arrays, providing a platform to investigate the influence of plasmonic structures on the lattice-induced plasmon dipoles responsible for the emergence of such domains. They also allow us to explore the coherent networks formed through the coupling of these domains and with their neighboring domains. The findings of this study offer an opportunity to examine the effects of micron-scale coherently extended plasmon states and their potential applications in the long-range coherent transport of energy and information.

DOI: 10.1103/PhysRevA.108.023512

I. INTRODUCTION

Recent investigations have focused on the application of surface lattice resonances (SLRs) in arrays of metallic nanoantennas for optical energy transport [1], long-range dipole-dipole interactions [2], and enhanced energy transfer through the Purcell effect [3]. Such resonances, which arise from the hybridization of localized surface plasmon resonances (LSPRs) with diffractive modes of lattices, offer other applications, including biological and chemical sensing [4–12], excitonic laser systems [13–15], optical filters [16], control of quantum emitter emission [13,15], perfect absorbers [17], and quantum information processing [18]. One unique application of SLRs lies in their ability to coherently excite lattice-induced dipole modes in one-dimensional arrays of Au nanoislands or Si nanocrystals and to facilitate the coupling of these dipoles to form networks of in-phase dipoles over long distances [19,20]. Such networks provide the opportunity to spread coherent information over ultralong-range distances.

The formation of SLRs in periodic arrays of regions containing metallic nanoparticles provides a unique platform for studying plasmonics and coherent-plasmonic processes [21–24]. Various techniques have been employed to fabricate such structures, including templated self-assembly of colloidal nanoparticles and nanorods [25], printing transfer [26], and soft lithography and template-assisted colloidal self-assembly [27]. Recently, we experimentally investigated the optical properties of periodic arrays of regions composed of densely packed Au nanoislands, where the sizes, shapes, and positions of the nanoislands exhibit random distributions [21,24]. We demonstrated that under specific conditions, these arrays, referred to as templated nanoisland arrays, can support a different type of SLR. This SLR arises from the coherent hybridization between the lattice-induced plasmon modes of the nanoislands and the diffraction modes of the arrays [21,24]. The presence of such resonances enables the coherent excitation and coupling of the plasmonic dipoles of the nanoislands, giving rise to plasmon modes that are coherently extended throughout the entire volume of each region, forming what we called phase-correlated dipole domains (PCDDs). Such domains, which can have footprints reaching up to one micron, can coherently couple with each other, giving rise to coherent networks of PCDDs spanning ultralong distances [21].

The main objective of this paper is to investigate the scattering processes driven by SLRs in templated nanoisland arrays and demonstrate how the coherent effects, represented by the formation of PCDDs and their networks, can be observed in the spectral and intensity features of the far-field scattering. To achieve this, we consider that the incident light reaches such arrays at a normal angle, but detect their scattering along their planes, i.e., perpendicular to the incident light (in-plane scattering). We show that such a scattering process carries the imprint of the coherent information associated with SLRs in the propagation directions, spectral features, and intensities of the in-plane scattering. This allows us to investigate how the sizes and shapes of the nanoislands influence the coherent signatures in the far-field scattering via

*seyed.sadeghi@uah.edu

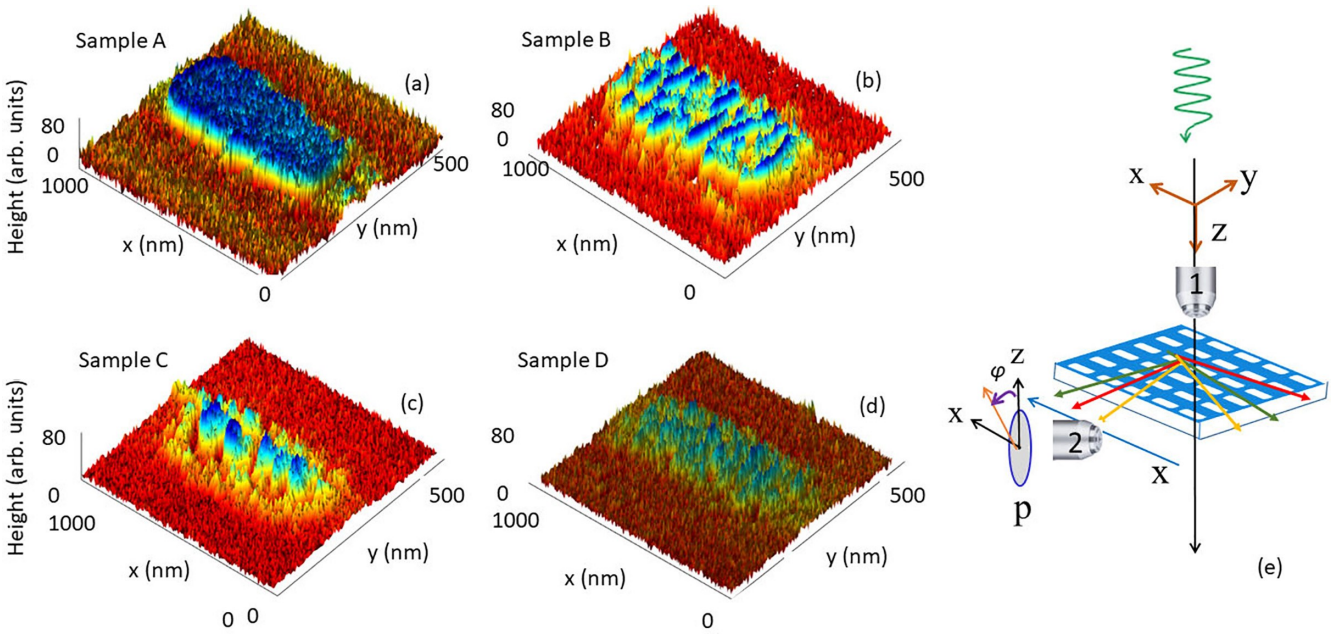

FIG. 1. (a)–(d) Close-up views of the SEM images of the Au plasmonic architecture of regions of samples A–D, respectively. (e) Schematic of the optical setup used to measure the in-plane scattering of the arrays. The templated nanoisland arrays are formed when the periodic open regions seen in (e) are replaced by the architectures shown in (a)–(d). "P" in (e) refers to a polarization analyzer.

PCDDs and their networks. To achieve this, by controlling the fabrication processes, we explore the impact of periodic templated arrays of regions with different plasmonic architectures [depicted in Figs. 1(a)–1(d)] on the far-field scattering. The obtained results provide a different platform for studying the physics of micron-scale coherently extended plasmon states and their long-range networks, with potential applications in energy and information transport, and quantum sensors. They can also be useful for the investigation of systems involving random phase metasurfaces [28] and strain-induced plasmon confinement via polycrystalline graphene [29].

II. EXPERIMENTAL AND SIMULATION METHODOLOGIES

In this study, we fabricated four types of templated samples using a specific process. The fabrication process began by creating masks with periodic open regions on glass substrates [see Fig. 1(e)]. These masks were formed by spin coating a resist material (ZEP520A) onto the glass substrates. Subsequently, electron-beam lithography was employed to expose designated regions of the resist in a periodic manner. Afterward, the exposed regions were chemically removed, resulting in periodic open areas with lateral dimensions of 800 × 200 nm. The separation between these areas, i.e., the lattice constants, along the x axis (a_x) and y axis (a_y), were 0.5 and 1 μm, respectively.

The next step involved depositing varying thicknesses of gold (5 to 20 nm) onto these masks using an evaporator. Subsequently, a chemical lift-off process was performed. Some of the samples were subjected to thermal annealing at 530 °C for 5 minutes. The combination of annealed and unannealed samples resulted in different nanoscale Au architectures, which are referred to here as plasmonic unit regions (URs).

Figures 1(a)–1(d) illustrate the metallic structures of these URs, with decreasing deposited gold thicknesses from 20 to 5 nm, respectively. Sample A [Fig. 1(a)] corresponds to the case with a 20 nm deposited gold thickness with ther-mal annealing. In this case, the URs remain as solid gold nanoantennas. Samples B [Fig. 1(b)] and C [Fig. 1(c)] have a deposited gold thickness of 10 nm. The former case was not annealed, while the latter was annealed under the same conditions as sample A. These cases exhibit intermediate characteristics, with connected nanoislands [Fig. 1(b)] and nearly separated nanoislands [Fig. 1(c)], respectively. Sample D [Fig. 1(d)] represents the case with a 5 nm gold deposition with annealing similar to samples A and C. In this case, the nearly isolated gold nanoislands within the URs are relatively small. In addition to these, samples with similar metallic structures as samples B–D, but without templating, were also fabricated. The scanning electron microscope (SEM) images of these samples, referred to as samples b2, c2, and d2, are shown in Figs. 2(a)–2(c), respectively. Note that Figs. 1(a)–1(d) are three-dimensional renders of SEM images of samples A–D, primarily intended for comparing the profile shapes of these samples.

Figure 1(e) illustrates the optical setup that was utilized to measure the extinction spectra and in-plane scattering of the samples. The experimental configuration involved the use of two microscope objectives: objective 1 with NA = 0.5 and objective 2 with NA = 0.85. Objective 1, with a nominal spot size of approximately 2 μm at 800 nm, was responsible for focusing the incident light into the arrays. On the other hand, objective 2 was employed to collect the scattered light along the edges of the glass substrates supporting the arrays with high resolution. To capture the in-plane scattering, objective 2 scanned across the entire length of the substrate side (20 mm) along both the x axis and y axis. For extinction measurements,

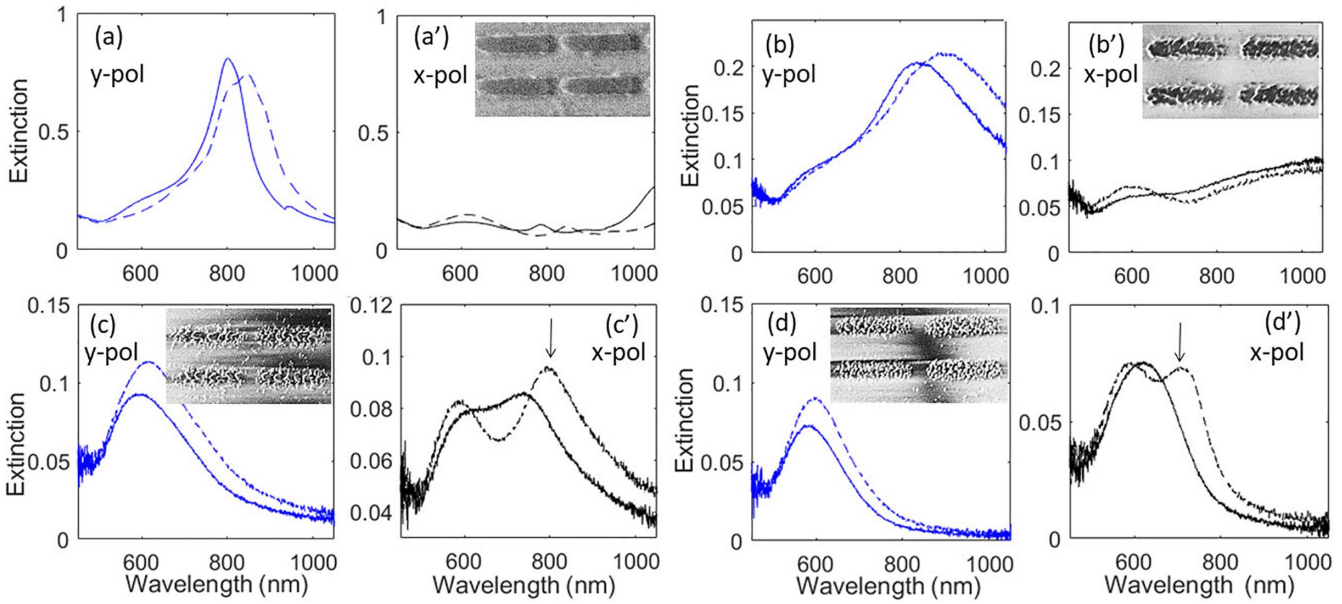

FIG. 2. Extinction spectra of samples A–D when the incident light is polarized along the (a)–(d) *y* axis and (a^0)–(d^0) *x* axis, respectively. The solid lines represent the case when the superstrate is air, while the dashed lines represent the case when the superstrate is methanol. Insets show the SEM images of the corresponding samples.

the transmitted light passing through the samples was utilized. The incident light was polarized along two orthogonal directions: the *x* axis (x-pol) and the *y* axis (y-pol). The light source used for these experiments was a halogen bulb with a peak intensity at approximately 750 nm. It is important to note that the regions containing the arrays had sizes of 200 × 200 μm, located near the center of the square glass substrate measuring 20 × 20 mm on each side.

To numerically investigate the concept of PCDDs and coherent inter-PCDD coupling, we utilized the finite-difference time-domain (FDTD) method provided by LUMERICAL. In this study, the unit cells (or URs) were represented by regions with a length of *L*, width of *W*, and height of *H*. Each region contained gold (Au) nanospheres with random sizes ranging from 5 to 20 nm, replicating the configuration of sample D. We applied periodic boundary conditions in the *x*-*y* plane of a UR. To prevent reflection along the *z* axis, we included a perfectly matched layer (PML) to suppress reflection from the boundary of the simulation domain. By analyzing the transmitted light intensity (T) through the sample, the extinction spectra were calculated as $1 - T$. The simulations corresponding to samples A–C have been reported elsewhere [21].

III. SURFACE LATTICE RESONANCES IN TEMPLATED NANOISLAND ARRAYS

In this paper, our primary focus is to investigate the coherent signatures, associated with the in-phase interaction of nanoparticles, in the far-field scattering of templated nanoisland arrays. In this section, we specifically aim to discuss experimental signatures of PCDDs and their networks. To begin, we present our results for the extinction spectra of samples A–D, which are also partially reported in Ref. [21]. Figures 2(a) and 2(a^0) depict the extinction spectra of sample A when the incident light is polarized along the *y* axis (y-pol) and *x* axis (x-pol), respectively. When the polarization is along the *x* axis, the spectra exhibit slight remnants of plasmonic multipolar features associated with the longitudinal modes of the nanoantennas [Fig. 2(a^0), solid line]. However, for y-pol, a sharp peak is observed at approximately 806 nm [Fig. 2(a), solid line]. This peak indicates the presence of SLRs [12,30–32], as discussed further in the following.

For sample B, the observed peak in the y-pol case [Fig. 2(b), solid line] is significantly broader compared to that in sample A. This broadening can be attributed to the fact that in sample B, the nanoantennas are fractured rather than solid [Fig. 1(b)]. Additionally, the broadening can be linked to the detuning of the LSPRs of this sample from the Rayleigh Anomaly (RA) wavelength. On the other hand, inspection of the extinction spectrum of sample B for x-pol [Fig. 2(b^0)] shows a distinct difference. Such a spectrum (solid line) does not have the characteristic features of multipolar LSPRs, but rather the LSPRs associated with the fractured nanoantennas. This indicates that the incident light with x-pol does not see the periodic nature of the array. In fact, the solid line in Fig. 2(b^0) resembles the response of untemplated nanoislands (Fig. 3). In particular, in the case of sample b2 [Fig. 3(a)], the response exhibits a monotonic rise with wavelength [Fig. 3(a^0)], similar to the solid line in Fig. 2(b^0). The slight kink at around 600 nm in Fig. 2(b^0) is associated with the impact of the lift-off process.

Note that the dashed lines in Fig. 2 represent the effect of increasing the refractive index of the superstrate by adding droplets of methanol on top of the arrays. Both Figs. 2(a) and 2(b) exhibit a clear redshift, which can be attributed to the redshift of both the LSPRs and RA wavelengths.

The results for samples C and D exhibit distinct characteristics that are different from samples A and B. In the case of sample C, the extinction spectrum for the y-pol polarization shows a single peak at approximately 594 nm

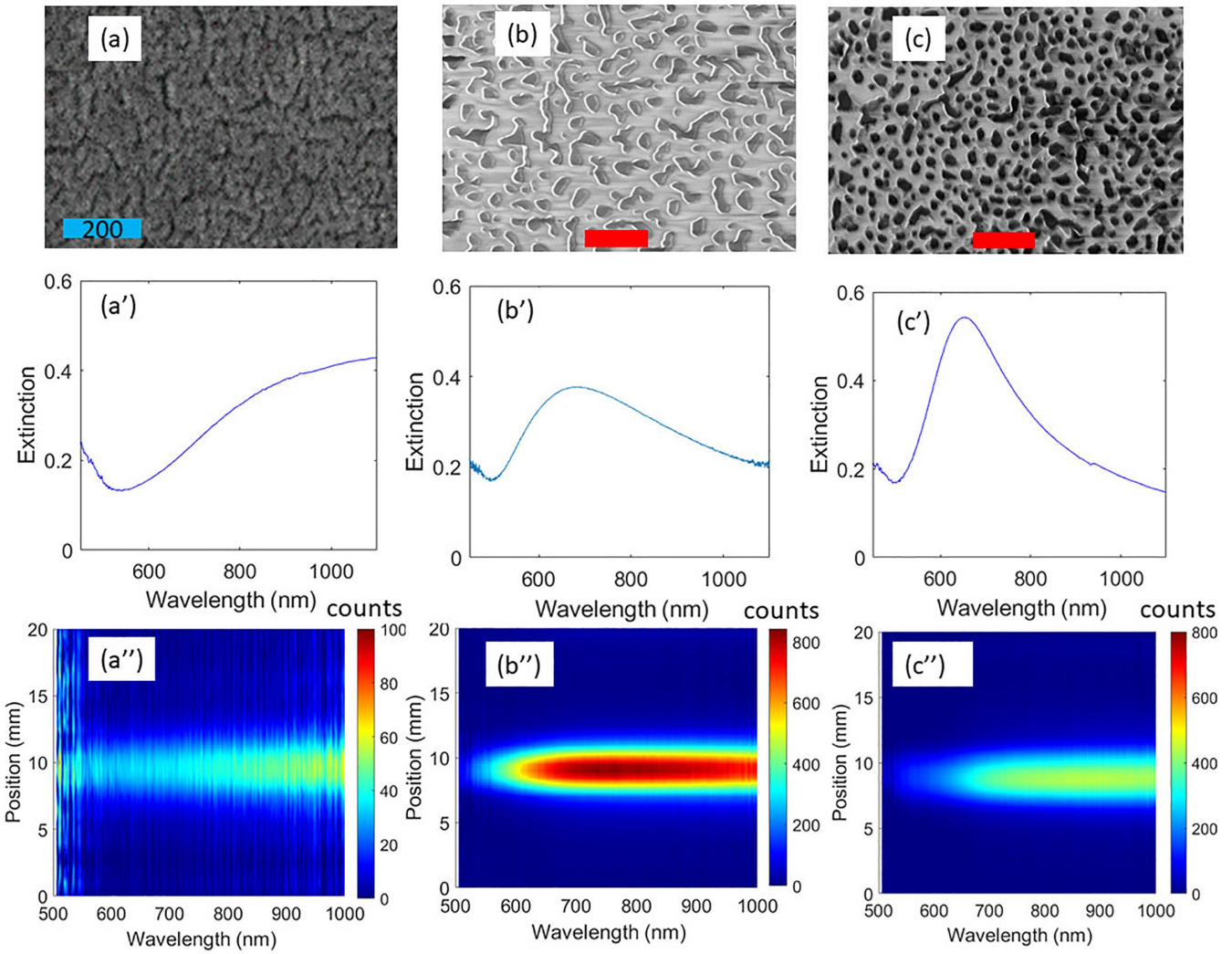

FIG. 3. (a)–(c) SEM images, (a^0)–(c^0) extinction spectra, and (a^{00})–(c^{00}) in-plane scattering, of samples b2, c2, and d2, respectively. In (a^{00}), (b^{00}), and (c^{00}), the color-coded bars, representing the in-plane scattering counts, range from 0 to 100, 0 to 800, and 0 to 800, respectively. The scale bar in (a) is 200 nm, and the scale bars in (b) and (c) are 1000 nm. Samples b2 and c2 both have 10 nm Au; sample d2 Au thickness is 5 nm. Samples c2 and d2 were thermally annealed.

[Fig. 2(c), solid line]. Such a spectral response is very similar to that of the untemplated sample c2 [Fig. 3(b)]. As shown in Fig. 3(b^0), such a sample also exhibits a broad LSPR peak, indicating that the optical response of sample C for the y-pol is not sensitive to the periodicity of the structures. In other words, such a response is influenced by the individual nanoislands rather than the collective response of the arrays as observed in samples A and B, where the y-pol response is associated with SLRs. The dashed line in Fig. 2(c) represents the impact of increasing the refractive index, which results in a simple redshift, a standard response observed in nanoislands.

The results of sample C for x-pol are even more distinct. As shown in Fig. 2(c^0), under this condition, the spectrum of this exhibits two partially overlapped peaks: one at 612 nm and the other at 740 nm (solid line). The addition of methanol to the superstrate makes these two peaks more distinct (dashed line). Under this condition, the shorter-wavelength peak undergoes minimal shifting, while the longer-wavelength peak (indicated by the arrow) experiences a significant shift. As discussed in the following, the longer peak is associated with a different form of SLR, originating from the coherent excitation of the nanoislands [21,24]. In this scenario, the nanoislands in each unit region (UR) are coherently coupled together, forming PCDDs. The addition of methanol creates a more uniform environment for the nanoislands, thereby enhancing their coherent excitation [7]. Note that for the case of the untemplated nanoisland arrays, the optical responses are found independent of the incident light polarization.

A similar situation is observed for sample D [Figs. 2(d) and 2(d^0)]. However, in this case, the plasmonic polarizabilities of the nanoislands in sample D are smaller compared to those in sample C, resulting in a less pronounced SLR when the superstrate is air [Fig. 2(d^0), solid line]. The addition of methanol clearly enhances the peak associated with this process (indicated by the arrow). For the y-pol polarization, similar to sample C, the response of sample D is predominantly influenced by the individual nanoislands [Fig. 2(d)]. This can be observed by considering the optical response of sample d2 [Fig. 3(c)]. In this case, the extinction spectrum

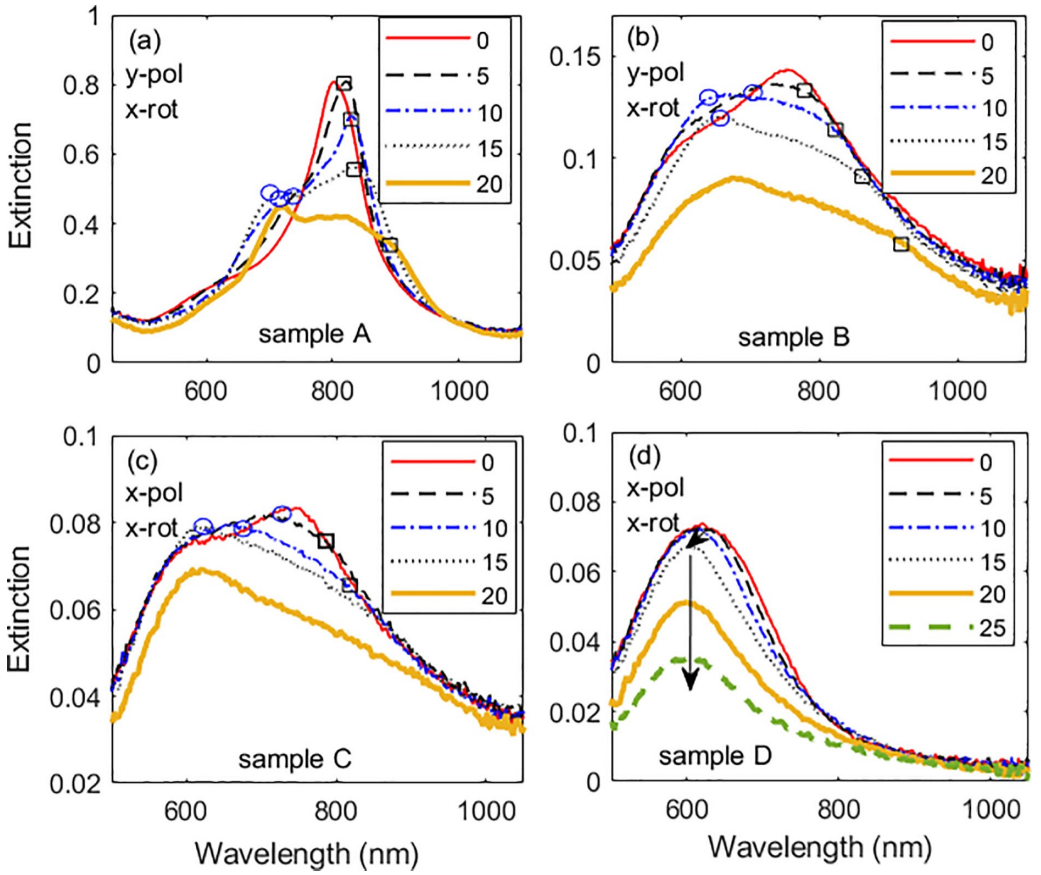

FIG. 4. (a)–(d) The extinction spectra of samples A–D with rotation about the *x* axis, respectively. In (a) and (b), the incident polarization was along the *y* axis (y-pol), while in (c) and (d), the incident light was polarized along the *x* axis (x-pol). The black squares and blue circles serve as guides for identifying the optical features associated with the $(-1, 0)$ and $(+1, 0)$ RA modes. The solid arrows in (d) are eye guides of variation of the peaks with angle of rotation. The legends show the angles of rotation in degrees.

becomes sharper due to the specific shapes and sizes of the nanoislands, leading to distinct optical features.

To discuss the nature of SLRs in samples A–D, the samples were rotated along the *x* and *y* axes, and variations in their extinction spectra were observed. Because of the hybridization of plasmon resonances with RA, under this condition the removal of the degeneracy of the RA modes splits these spectra [33]. Sample A provides a straightforward situation, as rotating the sample along the *x* axis for the y-pol resulted in the clear formation of peaks on both sides of the original peak [Fig. 4(a)]. This indicates a parallel coupling of RA with the LSPRs of the nanoantennas in this sample. Here, black squares and blue circles are used as visual aids to highlight the wavelengths associated with peaks corresponding to the $(-1, 0)$ and $(+1, 0)$ RA modes, respectively [24]. Sample B, however, exhibits a similar situation, although the presence of fractured nanoantennas in this sample has suppressed this process [Fig. 4(b)]. The addition of a thin layer of Si (10 nm), as shown in the Appendix (Fig. 11), further enhances these modes.

In the case of samples C and D, when the superstrate is air, the RA modes are more disguised [Figs. 4(c) and 4(d)]. However, for sample C, we can still observe traces of the removal of RA mode degeneracy (represented by black squares and blue circles). For sample D, with x-pol and rotation along the *x* axis, the spectral variations exhibit an initial relatively significant blueshift followed by the suppression of the peak, accompanied by a smaller amount of blueshift. If the polarization of the incident light changes to y-pol while keeping the rotation axis unchanged, the extinction spectrum mostly undergoes a suppression of amplitude (Appendix, Fig. 12). This further indicates that in this case, the incident light does not interact with the periodicity of the sample, and rotation has minimal spectral impact. In the subsequent section, we explore the SLRs associated with the peak designated with an arrow in Fig. 2(d^0) (sample D) numerically.

IV. PCDD AND INTER-PCDD VIA SURFACE LATTICE RESONANCES

To demonstrate the formation of PCDDs and the coherent inter-PCDD coupling associated with SLRs in templated nanoislands, we conducted numerical simulations using LUMERICAL 2020A software for sample D. The cases related to samples A–C have been discussed in Ref. [21]. We considered a random distribution of Au nanospheres with radii ranging from 5 to 20 nm [Fig. 5(a)]. These nanospheres were positioned within regions with dimensions of 800 nm in length and 200 nm in width, corresponding to the templated region (UR) regions in Fig. 1(d). The height of each region (H) was

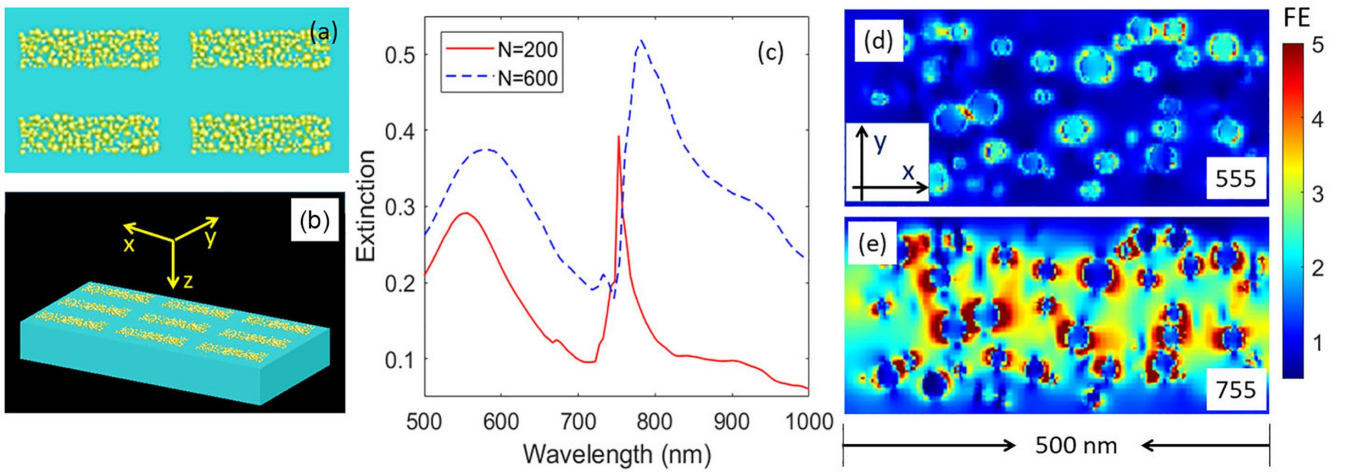

FIG. 5. (a) Top view and (b) oblique view of the periodic regions containing Au nanospheres with radii ranging from 5 to 20 nm. (c) Extinction spectra of such a structure for x-pol with $N = 200$ (solid line) and $N = 600$ (dashed line). (d) and (e) show the field enhancement factor in the x-y plane at 555 and 752 nm, respectively. The color-coded bar shows the range of the field enhancement factor (FE).

set to 100 nm. Our simulations considered two different values for the number of nanospheres (N) within each region, namely 200 and 600.

The positions of the nanospheres and their sizes were determined by the software. As shown in Figs. 5(a) and 5(b), the regions containing the nanospheres were periodically arranged with lattice constants $a_x = 1000$ nm and $a_y = 500$ nm, as in sample D. The substrate was assumed to be glass. The superstrate was also assigned a similar refractive index, imitating the conditions of sample D in the presence of methanol [Fig. 2(d^0), dashed line].

Figure 5(c) presents the results of the numerical simulations for the extinction spectra of such a structure [21]. It shows the formation of a broad peak at approximately 555 nm and a sharp peak at 755 nm for $N = 200$ (solid line). When N is increased to 600, corresponding to a threefold increase in the concentration of nanospheres, the shorter peak shifts to 583 nm, while the longer peak becomes broader and redshifted to 781 nm (dashed line). This broadening can be attributed to the packing and potential touching effects of the nanospheres. This trend helps explaining the experimental results observed in Figs. 2(c^0) and 2(d^0) (dashed lines).

Figures 5(d) and 5(e) provide close-up views (500 × 200 nm) of the field enhancement factors in one of the regions shown in Fig. 4(a). These factors are defined as the ratio of the field intensity in the presence of the nanoparticles to that in their absence. The close-up views are presented in the x-y plane for $N = 200$ at 555 nm [Fig. 4(d)] and 755 nm [Fig. 4(e)]. It is important to note that the x-y plane is located approximately 50 nm above the substrate, corresponding to half of the region's height ($H/2$).

Figure 5(d) clearly illustrates the near fields associated with the LSPRs of the nanospheres. The results also indicate some degree of field inside the nanospheres. However, except for cases where nanospheres are very close to each other, the near fields mostly represent plasmonic fields associated with individual nanoparticles with minimal internanoparticle coupling. In contrast to this, the case corresponding to the peak at 755 nm in Fig. 5(c) reveals a different scenario. In this case, significant field enhancement occurs, enabling efficient coupling among most of the nanospheres within a given region [Fig. 5(e)].

In Fig. 6, we examine the overall modal field enhancement factors associated with the 555 and 755 nm peaks observed in Fig. 5(c). The wider views of the field enhancement factors are shown in the x-y plane [Figs. 6(a) and 6(a^0)], the x-z plane [Figs. 6(b) and 6(b^0)], and the y-z plane [Figs. 6(c) and 6(c^0)]. At 555 nm, there is minimal interaction between the unit regions (URs), indicating individual excitation of the nanospheres [Figs. 6(a)–6(c)]. However, at 755 nm, the optical lattice modes between the URs become significant, as depicted in Figs. 6(a^0) and 6(b^0). These figures demonstrate how such modes efficiently form within the URs, highlighting the coherent coupling among them, leading to the formation of PCDDs. The interdomain coupling extends the coherent excitation across the entire regions of the URs along the x axis, forming a networks of PCDDs.

V. IN-PLANE SCATTERING VIA UNTEMPLATED NANOISLANDS

This paper explores the encoding of coherent information related to PCDDs and their networks into far-field scattering. To do this, we begin by analyzing the in-plane scattering characteristics of samples b2, c2, and d2, which represent untemplated nanoislands, lacking periodic features. The SEM images of these samples show that sample b2 primarily consists of a fractured Au (gold) thin film [Fig. 3(a)], as the case of sample B. In the case of sample c2, the nanoislands seem to be separated, but possess highly irregular shapes and sizes, as shown in Fig. 3(b). On the other hand, sample d2 exhibits more isolated nanoislands [Fig. 3(c)], similar to the case of sample D. Figures 3(a^0)–3(c^0) display the corresponding transition of extinction spectra for these samples, with more localized plasmons leading to a sharper blueshifted peak.

Figures 3(a^{00})–3(c^{00}) depict the in-plane scattering observed on one side of the glass substrates supporting the nanoislands. The results indicate that sample c2 exhibits the most intense

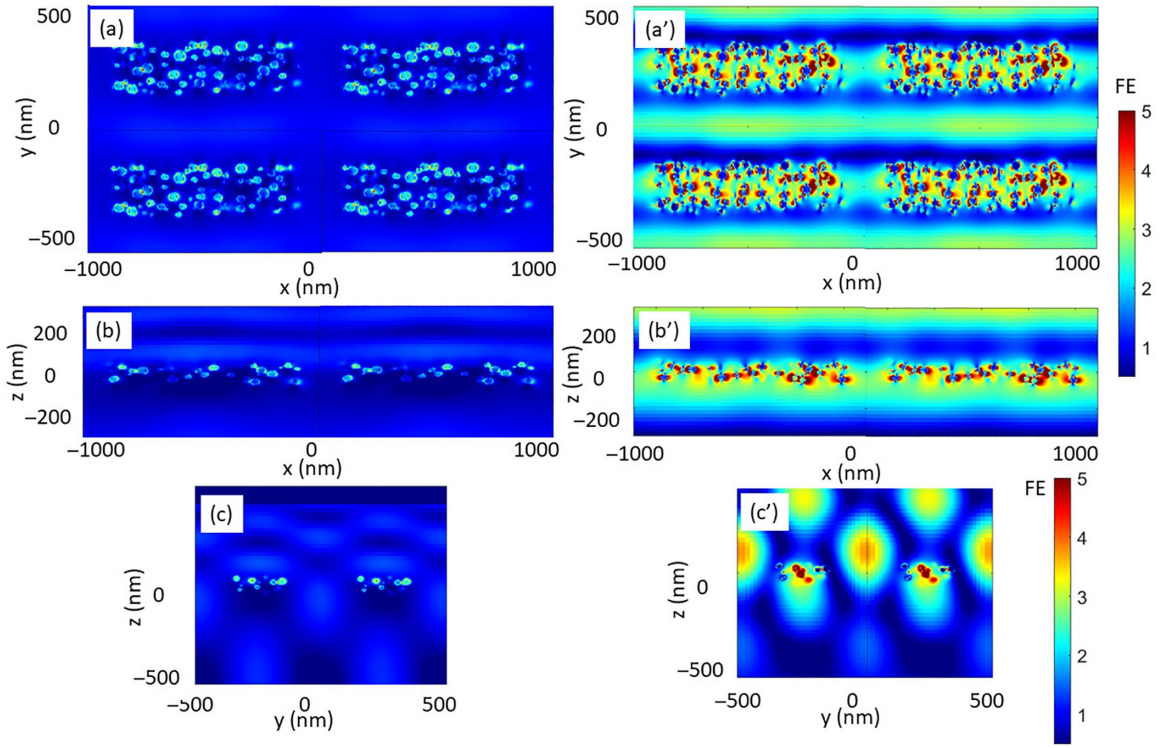

FIG. 6. Mode field enhancement profiles of four adjacent URs of the periodic structure shown in Fig. 4(a) at (a)–(c) 555 nm and (a^0)–(c^0) 755 nm. (a) and (a^0) show the field enhancement factor in the *x*-*y* plane, (b) and (b^0) in the *x*-*z* plane, and (c) and (c^0) in the *y*-*z* plane. Here the incident field is considered to be polarized along the *x* axis (x-pol). The color-coded bars show the ranges of the field enhancement factor (FE).

in-plane scattering, spanning over a spectral range starting from approximately 500 nm [Fig. 3(b^{00})]. On the other hand, sample d2 displays significantly lower scattering compared to sample c2 [Fig. 3(c^{00})]. Sample b2 exhibits the least amount of in-plane scattering [Fig. 3(a^{00})]. It should be noted that the scale bar representing the scattering count ranges from 0 to 100 for Fig. 3(a^{00}), while for Figs. 3(b^{00}) and 3(c^{00}), the range is between 0 and 800. Despite the significant variations in intensity, all three samples exhibit similar scattering spectral patterns.

The underlying reasons behind the observed in-plane scattering in Fig. 3 can be attributed to the inhomogeneity of the medium of the systems, which include Au nanoislands placed on the glass substrates with air as a superstrate. In such a configuration, as shown in Refs. [34] and [35], a certain level of coupling is expected between the scattering of the nanoislands and the substrate. In fact, based on the results shown in Figs. 3(a^{00})–3(c^{00}), this scattering occurs over a wide range of the spectrum, resembling the spectrum of the incident light. The scattering of the systems studied in this section have some similarities to those of random phase metasurfaces [28] and strained polycrystalline graphene structures [29].

VI. COHERENT AMPLIFICATION FAR-FIELD SCATTERING VIA SLR

To investigate PCDDs and their long-range coherent coupling using far-field in-plane scattering, we first examine the influence of SLRs on the scattering process in arrays with regular nanoantennas, focusing specifically on sample A. When incident light is polarized along the *y* axis (y-pol), the diffraction coupling along the same axis gives rise to the formation of SLRs. This happens since the transverse LSPRs of these nanoantennas are closely located to the RA wavelength, allowing them to become hybridized [Fig. 2(a)]. However, for incident light polarized along the *x* axis (x-pol), the scattering process primarily involves the longitudinal LSPRs of individual nanoantennas [Fig. 2(a^0)].

Figure 7(a) displays the in-plane scattering detected along the *x* axis (thick one-sided arrow) for x-pol (two-sided arrow). The results exhibit a distinct spectral profile that differs significantly from the scattering detected along the *y* axis for the same incident light polarization [Fig. 7(b)]. Specifically, the x-pol scattering predominantly shows a single peak at approximately 955 nm. In contrast, the y-pol scattering reveals two peaks, one at 780 nm and the other at 910 nm. It is important to note that for x-pol, although the scattering spectrum primarily reflects the behavior of individual nanoantennas' LSPRs, their in-plane scattering behavior is influenced by the presence of neighboring nanoantennas within the array [36].

Figures 7(c) and 7(d) depict the in-plane scattering along the *x* axis and *y* axis, respectively, when the incident light is polarized along the *y* axis (y-pol). These results demonstrate significantly enhanced scattering compared to the x-pol cases [Figs. 7(a) and 7(b)]. In the case of detection along the *x* axis, the scattering peak occurs at 882 nm, while for detection along the *y* axis, it occurs at 866 nm. The latter presents the maximum amount of scattering.

The high counts observed in Figs. 7(c) and 7(d) (indicated by the numbers on top of each peak) indicate the influence

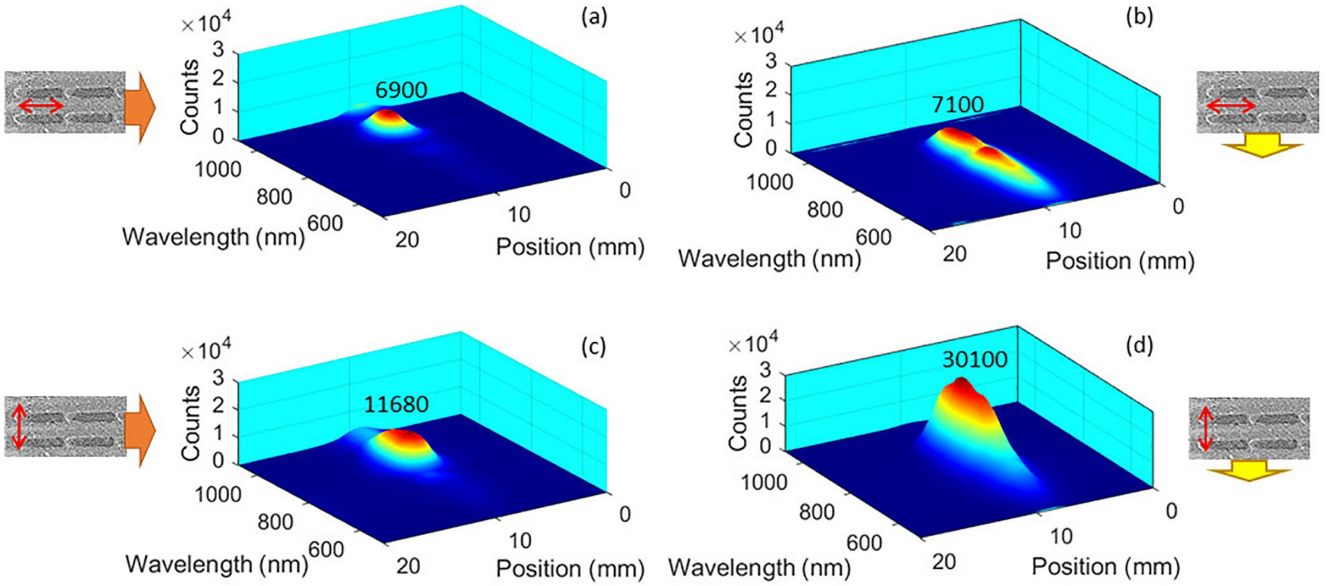

FIG. 7. In-plane scattering of sample A along the (a) x axis and (b) y axis for x-pol. (c) and (d) are similar to (a) and (b), respectively, but for y-pol. The images to the right or to the left show a small portion of the SEM image of this sample, wherein the two-sided arrows represent the polarization directions of the incident light and the one-side wide arrows refer to the propagation directions of the in-plane scattering. The numbers on the top of each peak represent the maximum counts of the scattering associated with the peaks.

of SLR on the in-plane scattering process. Indeed, the results in Figs. 7(b) and 7(d) demonstrate that switching the incident light polarization from x-pol to y-pol leads to approximately a 4.5-fold increase in the in-plane scattering intensity. This scattering enhancement process is an indication of coherent processes associated with the formation of SLR. It is important to note that SLR involves the coherent excitation of the LSPRs of individual nanoantennas, which establishes a direct phase relationship between diffracted optical fields in the arrays and plasmon resonances of the nanoantennas [30].

To perform polarization analysis of the scattering light, a polarization analyzer (P) was positioned at the back of objective 2, with its axis oriented at an angle φ relative to the z axis, as illustrated in Fig. 1(e). The light passing this analyzer was then guided to the spectrometer. When φ is 0°, the axis of the polarization analyzer is vertical, aligned along the z axis. Conversely, when φ is 90°, the axis of the polarization analyzer is horizontal, perpendicular to the z axis. By varying the angle φ, the polarization analyzer can assess the polarization-dependent properties of the in-plane scattering from the samples.

The results obtained from the polarization analysis of the in-plane scattering for x-pol and y-pol of sample A reveal interesting findings. For x-pol, when the scattering is detected along the x axis, the polarization of the scattered light appears to be mixed, as shown in Fig. 8(a). This is evident from the fact that the scattered light exhibits components for both $\varphi = 0^\circ$ (solid line) and $\varphi = 90^\circ$ (dashed black line). In other words, the scattered light consists of a combination of polarization states along both the vertical and horizontal directions. However, when the incident light polarization remains unchanged and the scattering is detected along the y axis, the scattered light demonstrates nearly complete linear polarization along the z axis, as illustrated in Fig. 8(b) (solid orange line). This means that the scattered light becomes predominantly polarized in the vertical direction, parallel to the z axis.

A similar situation occurs for y-pol, with the exception that the scattered light becomes nearly purely polarized horizontally, corresponding to $\varphi = 0^\circ$ [Fig. 8(d)]. In this case, the scattered light is predominantly polarized in the horizontal direction, perpendicular to the z axis. For the same incident

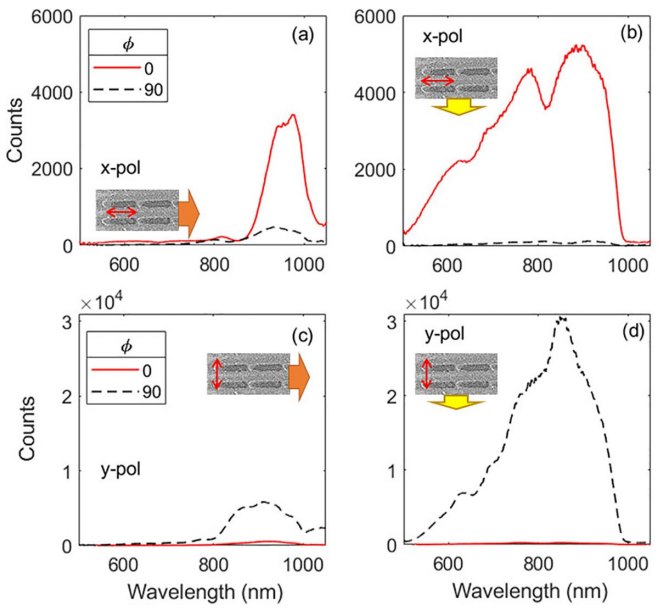

FIG. 8. Polarization analysis of the in-plane scattering of sample A when the incident light is polarized along the (a),(b) x axis and (c),(d) y axis. Here, $\varphi = 0^\circ$ and 90° refer to the case when the axis of the polarization analyzer is parallel and perpendicular to the z axis, respectively.

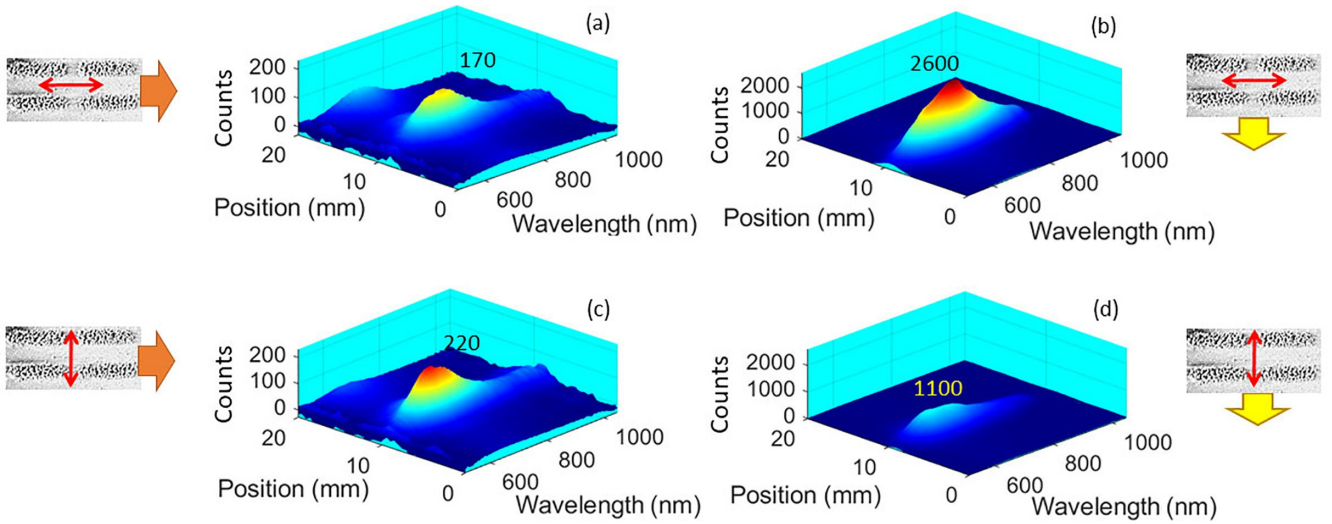

FIG. 9. In-plane scattering of sample D for x-pol when scattering is detected along the (a) x axis and (b) y axis. (c) and (d) are similar to (a) and (b), respectively, but for y-pol. The images to the right and left show small portions of the SEM image of the sample, wherein the two-sided arrows represent the polarization directions of the incident light, and the wide one-sided arrows represent the propagation direction of the in-plane scattering.

polarization but detection along the x axis, the situation resembles that depicted in Fig. 8(a), where the scattered light exhibits mixed polarization states along both the vertical and horizontal directions.

The results obtained for sample B exhibit a similar trend, although the fractured nature of the nanoantennas in this sample [Fig. 1(b)] compromises the sharpness of its features. This leads to a reduction in the scattering intensities and

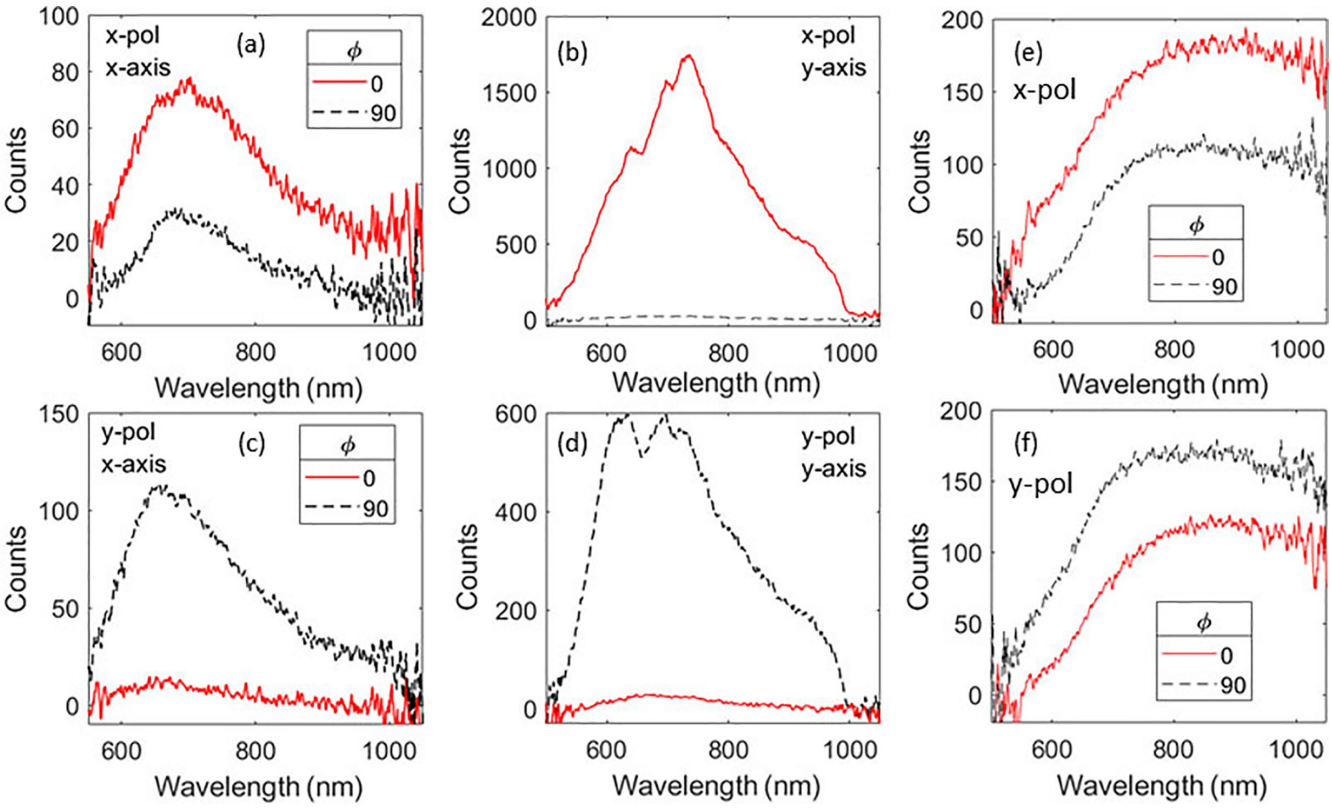

FIG. 10. The polarization analysis of the in-plane scattering of sample D with the incident light polarized along (a),(b) the x axis or along (c),(d) the y axis. In (a) and (c), the scattering is detected along the x axis, while in (b) and (d), it is detected along the y axis. (e) and (f) represent the polarization of in-plane scattering for sample d2 with x-pol and y-pol. Here, $\varphi = 0^\circ$ and 90° indicate the cases when the axis of the polarization analyzer was parallel and perpendicular to the z axis, respectively.

polarization characteristics of the sample, as shown in Appendix (Fig. 13). Due to the plasmonic structure of this sample, the coherent processes associated with SLRs are suppressed. This suppression significantly affects the polarization properties of the scattered light. In fact, as shown in Appendix (Fig. 14), the scattered light of this sample exhibits strong polarization mixing. This is particularly notable for the case of x-pol with detection along the x axis, wherein sample B demonstrates nearly unpolarized scattering.

VII. SIGNATURES OF PCDDs AND THEIR COHERENT COUPLING IN THE IN-PLANE SCATTERING

The results shown in Fig. 7 demonstrate the coherent amplification of in-plane scattering through SLRs in an array supporting the LSPRs associated with solid nanoantennas. However, the cases of samples C and D present different situations, as they involve periodic regions containing nanoislands with much smaller dimensions compared to the nanoantennas in sample A. In this section, we further investigate the application of SLRs to gain insights into the formation of PCDDs and their long-range coupling. While sample D is specifically examined, it is important to note that sample C exhibits similar characteristics with some spectral and intensity variations.

Figure 9 presents the results of in-plane scattering for sample D under x-pol [Figs. 9(a) and 9(b)] and y-pol [Figs. 9(c) and 9(d)]. These results exhibit contrasting features compared to the case of sample A (Fig. 7). One prominent effect observed in sample D is the significantly larger amount of scattering detected along the y axis for x-pol, as shown in Fig. 9(b). In contrast, for y-pol, the scattering is minimal, as depicted in Fig. 9(d).

These findings are consistent with the numerical simulation results presented in Figs. 5 and 6. Specifically, Figs. 6(a^0)–6(c^0) demonstrate that for sample D and x-pol, both PCDDs and effective inter-PCDD coupling (coherent networks) are strongly supported. Thus, Fig. 9(b) represents an enhancement of SLRs in far-field scattering induced by PCDDs. On the other hand, when the incident light is polarized along the y axis, the scattering process is expected to be associated with individual nanoislands, as shown in Fig. 9(d). It should be noted that similar to the case of solid nanoantennas, the scattering of such nanoislands is influenced by the presence of other neighboring nanoisland regions [36].

The results depicted in Figs. 9(a) and 9(c) indicate that when the scattering is detected along the x axis, regardless of the polarization of the incident light, the amount of scattering remains low. This observation suggests that the scattering associated with PCDDs and their networks is most efficient for directions perpendicular to the axis of these networks. In other words, the scattering processes related to such networks (and PCDDs) exhibit a preferred orientation perpendicular to their axes. This alignment enhances the interaction of the incident light with the PCDDs and facilitates efficient scattering along the y axis.

The results of the polarization analysis for the in-plane scattering of sample D are presented in Figs. 10(a)–10(d). These findings exhibit different features compared to sample A. When the scattering is detected along the x axis with x-polarized incident light, the polarization appears to be mixed,

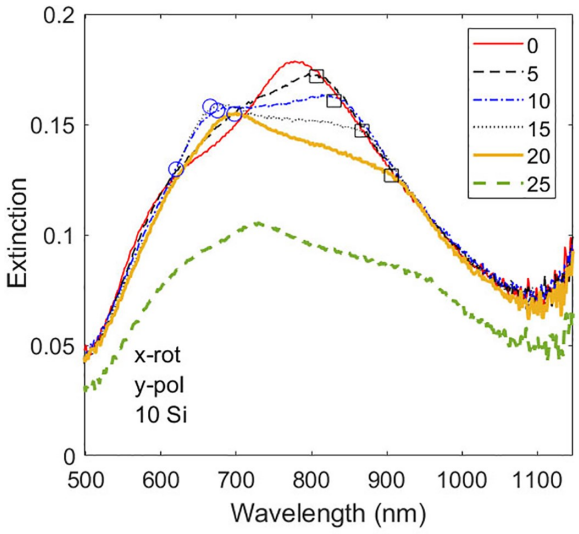

FIG. 11. Variations of extinction spectra of sample B under rotation along the x axis for y-pol when a layer of Si with 10 nm thickness is deposited on the top of the array. The numbers in the legends refer to the angles of rotation in degrees.

with peaks around 690 nm [Fig. 10(a)]. Conversely, when maintaining the incident light polarization as x-pol and detecting scattering along the y axis, a high degree of linear polarization is observed with significantly higher intensity [Fig. 10(b)]. It is noteworthy that minimal scattering is observed at $\varphi = 90^\circ$ (dashed black line), while a strong peak at 730 nm is observed at $\varphi = 0^\circ$ (solid orange line). This suggests that PCDDs and their networks actually maintain polarization, similar to the case of solid Au nanoantennas. On the other hand, for the y-pol, the in-plane scattering appears to become partially linearly polarized [Figs. 10(c) and 10(d)].

Considering the fact that the results presented in Fig. 10(b) occur for a structure consisting of templated nanoislands emphasizes the degree of coherent correlation established by

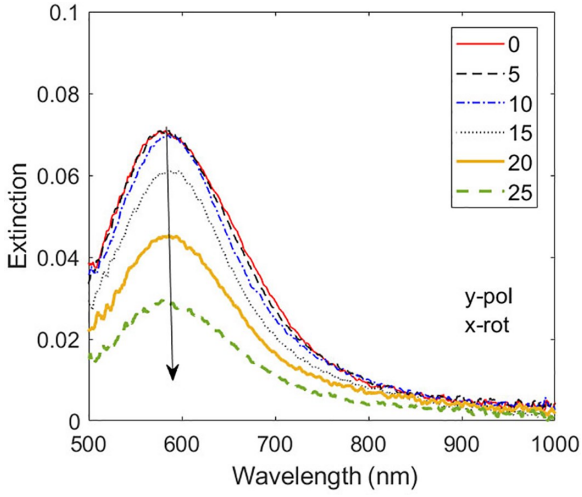

FIG. 12. Variations of the extinction spectra of sample D for y-pol and rotation along the x axis. The inset shows the angles of rotation in degrees. The solid arrow is the eye guide for the decrease of peaks of spectra as a function of this angle.

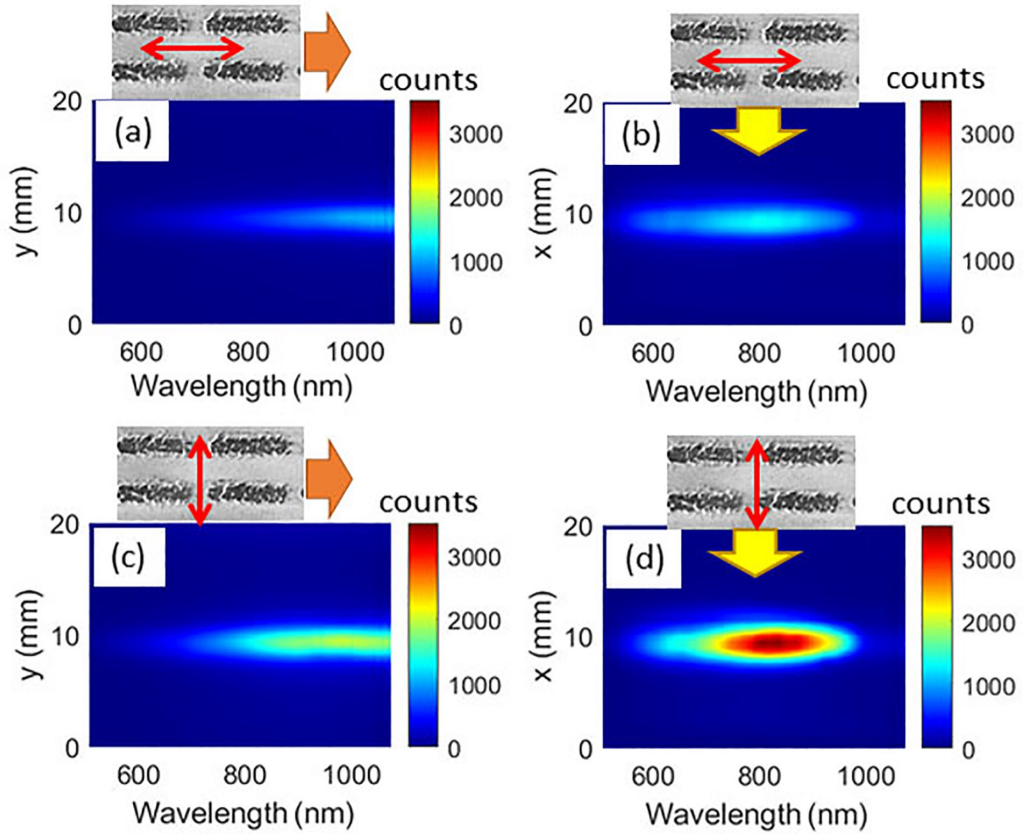

FIG. 13. In-plane scattering of sample B for x-pol when scattering is detected along the (a) *x* axis and (b) *y* axis. (c) and (d) are similar to (a) and (b), respectively, but for y-pol. The images on the top of each panel show small portions of the SEM image of the sample, wherein the two-sided arrows represent the polarization directions of the incident light and the wide one-sided arrows represent the propagation direction of the in-plane scattering. The color-coded bars refer to the counts of scattering.

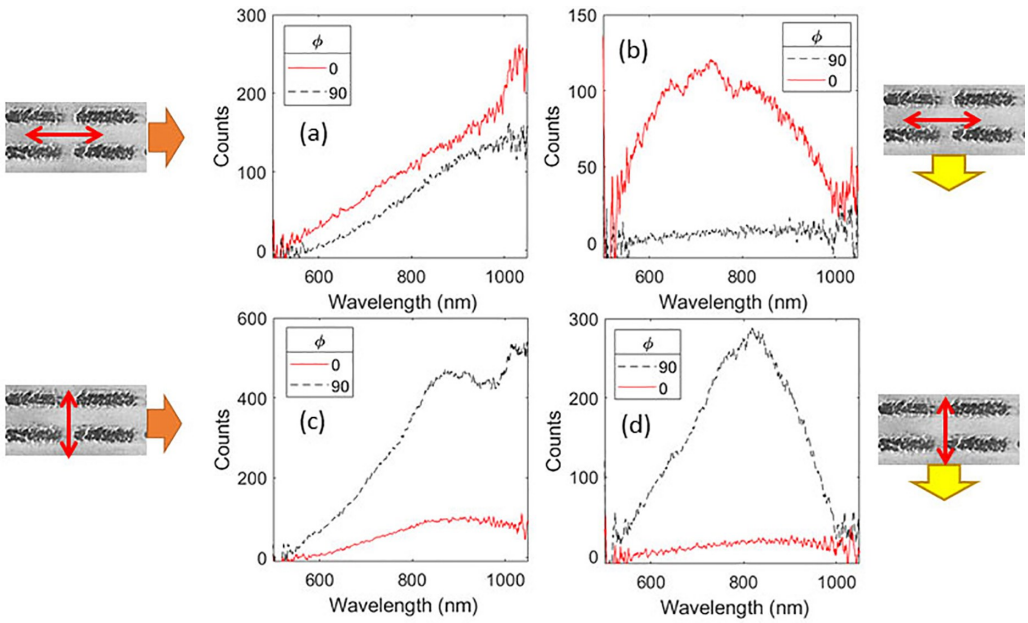

FIG. 14. Polarization analysis of the in-plane scattering of sample B when the incident light is polarized along the (a),(b) *x* axis and (c),(d) *y* axis. Here, $\varphi = 0^\circ$ and 90° refer to the case when the axis of the polarization analyzer is parallel and perpendicular to the *z* axis, respectively.

PCDDs and their networks. To assess the significance of this, we present the results for sample d2 in Figs. 10(e) and 10(f), which correspond to the scattering from the untemplated regions of nanoislands [Fig. 3(c)] for x-pol and y-pol configurations, respectively. In these figures, the spectral features for different φ angles are relatively similar for both x-pol and y-pol cases. The observed differences may be attributed to the influence of incident light polarization on the coupling of scattered light into the glass substrate.

Considering these findings, Figs. 10(e) and 10(f) indicate nearly unpolarized scattering. This polarization conversion process stands in stark contrast to the results shown in Fig. 10(b). These results highlight the fact that when nanoislands are templated, as in sample D, the coherent coupling via SLRs can profoundly alter the in-plane scattering properties. In other words, we are dealing with scattering associated with PCDD modes and inter-PCDD coupling, which result in nearly linearly polarized scattering.

VIII. CONCLUSIONS

We studied the utilization of far-field in-plane scattering from periodic arrays of regions containing nanoislands to investigate the formation of spatially delocalized plasmon resonances known as PCDDs. Our results demonstrated the coherent coupling of plasmonic resonances induced by the lattice, which extended over areas much larger than the spatial extent of individual nanoislands. We showed that the formation of phase-correlated dipole domains and their coherent coupling can be characterized through the measurement of scattered light within the plane of the substrates supporting these arrays. The interdomain coupling establishes a coherent network where coherent information is propagated over ultralong distances, spanning beyond several micrometers.

ACKNOWLEDGMENTS

This work is supported by the U.S. National Science Foundation under Grant No. ECCS-1917544.

APPENDIX

This Appendix includes Figs. 11–14, as described in the main text.

[1] R. K. Yadav, M. Otten, W. Wang, C. L. Cortes, D. J. Gosztola, G. P. Wiederrecht, S. K. Gray, T. W. Odom, and J. K. Basu, Nano Lett. **20**, 5043 (2020).
[2] A. K. Boddeti, J. Guan, T. Sentz, X. Juarez, W. Newman, C. Cortes, T. W. Odom, and Z. Jacob, Nano Lett. **22**, 22 (2022).
[3] R. Collison, J. B. Pérez-Sánchez, M. Du, J. Trevino, J. Yuen-Zhou, S. O'Brien, and V. M. Menon, ACS Photon. **8**, 2211 (2021).
[4] R. R. Gutha, S. M. Sadeghi, C. Sharp, and W. J. Wing, Nanotechnology **28**, 355504 (2017).
[5] X. Zhang, S. Feng, J. Zhang, T. Zhai, H. Liu, and Z. Pang, Sensors **12**, 12082 (2012).
[6] B. D. Thackray, V. G. Kravets, F. Schedin, G. Auton, P. A. Thomas, and A. N. Grigorenko, ACS Photonics **1**, 1116 (2014).
[7] B. Auguié and W. L. Barnes, Phys. Rev. Lett. **101**, 143902 (2008).
[8] Y. Sonnefraud, N. Verellen, H. Sobhani, G. A. Vandenbosch, V. V. Moshchalkov, P. Van Dorpe, P. Nordlander, and S. A. Maier, ACS Nano **4**, 1664 (2010).
[9] E. M. Hicks, X. Zhang, S. Zou, O. Lyandres, K. G. Spears, G. C. Schatz, and R. P. Van Duyne, J. Phys. Chem. B **109**, 22351 (2005).
[10] J. Li, J. Ye, C. Chen, L. Hermans, N. Verellen, J. Ryken, H. Jans, W. Van Roy, V. V. Moshchalkov, L. Lagae *et al.*, Adv. Opt. Mater. **3**, 176 (2015).
[11] S. M. Sadeghi, W. J. Wing, and Q. Campbell, J. Appl. Phys. **119**, 244503 (2016).
[12] S. M. Sadeghi, R. R. Gutha, and W. J. Wing, Opt. Lett. **41**, 3367 (2016).
[13] R. Guo, S. Derom, A. Väkeväinen, R. van Dijk-Moes, P. Liljeroth, D. Vanmaekelbergh, and P. Törmä, Opt. Express **23**, 28206 (2015).
[14] M. Ramezani, G. Lozano, M. A. Verschuuren, and J. Gómez-Rivas, Phys. Rev. B **94**, 125406 (2016).
[15] X. Yuan, L. Shi, Q. Wang, C. Chen, X. Liu, L. Sun, B. Zhang, J. Zi, and W. Lu, Opt. Express **22**, 23473 (2014).
[16] R. R. Gutha, S. M. Sadeghi, C. Sharp, A. Hatef, and Y. Lin, J. Appl. Phys. **125**, 023103 (2019).
[17] N. Liu, M. Mesch, T. Weiss, M. Hentschel, and H. Giessen, Nano Lett. **10**, 2342 (2010).
[18] R. J. Bettles, S. A. Gardiner, and C. S. Adams, Phys. Rev. Lett. **116**, 103602 (2016).
[19] S. M. Sadeghi and R. R. Gutha, Appl. Mater. Today **22**, 100932 (2021).
[20] S. M. Sadeghi and R. R. Gutha, Adv. Photon. Res. **2**, 2000129 (2021).
[21] S. M. Sadeghi and R. R. Gutha, Phys. Rev. Appl. **15**, 034018 (2021).
[22] L. Scarabelli, D. Vila-Liarte, A. Mihi, and L. M. Liz-Marzán, Acc. Mater. Res. **2**, 816 (2021).
[23] A. D. Utyushev, V. I. Zakomirnyi, and I. L. Rasskazov, Rev. Phys. **6**, 100051 (2021).
[24] S. M. Sadeghi, R. R. Gutha, and C. Sharp, J. Mater. Chem. C **7**, 9678 (2019).
[25] P. Molet, N. Passarelli, L. A. Pérez, L. Scarabelli, and A. Mihi, Adv. Opt. Mater. **9**, 2100761 (2021).
[26] C. Hanske, M. B. Muller, V. Bieber, M. Tebbe, S. Jessl, A. Wittemann, and A. Fery, Langmuir **28**, 16745 (2012).
[27] V. Gupta, P. T. Probst, F. R. Goßler, A. M. Steiner, J. Schubert, Y. Brasse, T. A. Konig, and A. Fery, ACS Appl. Mater. Interfaces **11**, 28189 (2019).
[28] A. Pors, F. Ding, Y. Chen, I. P. Radko, and S. I. Bozhevolnyi, Sci. Rep. **6**, 28448 (2016).
[29] S. Zanotto, L. Bonatti, M. F. Pantano, V. Mišeikis, G. Speranza, T. Giovannini, C. Coletti, C. Cappelli, A. Tredicucci, and A. Toncelli, ACS Photon. **10**, 394 (2023).
[30] V. G. Kravets, A. V. Kabashin, W. L. Barnes, and A. N. Grigorenko, Chem. Rev. **118**, 5912 (2018).

[31] R. R. Gutha, S. M. Sadeghi, and W. J. Wing, Appl. Phys. Lett. **110**, 153103 (2017).
[32] S. M. Sadeghi, W. Wing, and Q. Campbell, J. Appl. Phys. **119**, 114307 (2016).
[33] S. Rodriguez, G. Lozano, M. Verschuuren, R. Gomes, K. Lambert, B. De Geyter, A. Hassinen, D. Van Thourhout, Z. Hens, and J. G. Rivas, Appl. Phys. Lett. **100**, 111103 (2012).
[34] M. Schmid, R. Klenk, M. C. Lux-Steiner, M. Topič, and J. Krč, Nanotechnology **22**, 025204 (2011).
[35] H. Nishi and T. Tatsuma, ACS Appl. Nano Mater. **2**, 5071 (2019).
[36] J. Lin, J. B. Mueller, Q. Wang, G. Yuan, N. Antoniou, X.-C. Yuan, and F. Capasso, Science **340**, 331 (2013).